JARS Journal of Applied Remote Sensing

RESEARCH PAPER

Out-of-field stray light correction in optical instruments: the case of Metop-3MI

Lionel Clermont* and Céline Michel
Université de Liège, STAR Institute, Centre Spatial de Liège, Liège, Belgium

ABSTRACT. In high performance optical instruments, post-processing methods are employed to reduce the stray light (SL) level below what can be achieved by design. Often, algorithms are limited to SL coming from sources located inside the field of view (FOV) of the instrument; however, SL could also come from sources located outside the FOV. We describe a method for correcting out-of-field SL, in particular for the case of the Earth observation instrument Metop-3MI. The proposed approach is a variant of the in-field (IF) method developed previously. We estimate the out-of-field SL by a linear combination of the SL kernels modulated by the input scene radiance. The correction is computed for fields on a regularly spaced polar grid, providing reasonable variations of the solid angle sustained around individual fields. Compared with the case of IF SL correction, a difficulty is that the out-of-field input radiance is unknown. We implement a mirroring technique, which is shown to be effective in most situations. This method will be used to correct the in-flight data of Metop-3MI, hence providing an SL level sufficiently low to fulfill the mission requirement.

 [DOI: 10.1117/1.JRS.18.016508]

Keywords: stray light; out-of-field; Earth observation; correction algorithm

Paper 230310G received Jun. 28, 2023; revised Jan. 24, 2024; accepted Feb. 13, 2024; published Mar. 4, 2024.

1 Introduction

Stray light (SL) is a critical aspect for the development of space optical instruments. The first approach for SL control consists of optimizing the opto-mechanical design, e.g., with the use of baffles or anti-reflection coatings.[1,2] However, it is not always possible to reach satisfactory performance by design only, in which case a post processing correction is necessary. Methods have been developed to remove SL from an image based on prior calibration of the SL pattern as a function of the source position in the field of view (FOV).[3–5] For a given scene observed by the instrument, the SL is estimated and subtracted from the measured image to get the SL free image. For example, this principle is used for SL correction of Earth observation instruments such as POLDER,[3] Metop-3MI[5–7] or Flex.[8] A similar approach can also be applied to spectrographs or hyperspectral instruments for the correction of spectral SL.[9–11] In the most demanding situations, SL must be calibrated for many positions of the source in the field. As this is not always possible in practice, calibration on a restricted grid and interpolation of the maps at intermediate fields are necessary. For that purpose, an interpolation method was proposed for 3MI based on a local symmetry assumption.[5] Spatial and field binning can be applied to reduce the quantity of data, with consequences on the performance.[5]

In most situations, correction algorithms only consider SL caused by sources located inside the FOV of the instrument, called in-field (IF) SL. However, SL can also come from sources located outside the FOV, called out-of-field (OOF) SL. A front baffle is an effective way to

*Address all correspondence to Lionel Clermont, lionel.clermont@uliege.be

1931-3195/2024/$28.00 © 2024 SPIE

control OOF SL by design as it blocks out-of-field illumination outside the instrument. However, its effectiveness is directly related to its length, which is constrained by the total volume and weight available for the payload. A field stop is another method for OOF SL control, but it requires an intermediary focal plane, which is not present in all instruments. If the OOF SL level is beyond the user requirements, a correction algorithm must be implemented, too. Compared with the case of IF SL, a difficulty of OOF correction is that we do not know the input scene illuminating the instrument for sources located outside the FOV.

The thermal infrared sensor (TIRS) onboard Landsat 8 is an example of an instrument in which unexpectedly high OOF SL was discovered after the launch of the payload.[12] Montanaro et al.[12–14] developed a correction method based on simulations of OOF SL, with a model that was fine-tuned based on in-flight OOF SL measurements with the moon as a calibration source. The problem of OOF SL is conceptually similar to out-of-range (OoR) spectral SL in spectrographs. In that case, only the signal for wavelengths inside the instrument spectral range is measured, making it difficult to deduce the OoR SL. In the case of one-dimensional spectrographs, Nevas et al.[15] proposed deducing the OoR SL by simple extrapolation of the spectra.

In this paper, we describe an OOF SL correction method developed specifically for the Earth observation instrument 3MI.[16–18] The 3MI instrument has an on-axis refractive configuration with an optical FOV of 57 deg [Fig. 1(a)]. It will observe the Earth from a polar orbit, enabling a daily revisit time. The objective of the mission is to study the composition of the atmosphere, including the presence of aerosols. Operating in the visible and near infrared, spectral selection is done with a filter wheel. 3MI features a square detector array with $N \times N$ pixels ($N = 512$). The detector encircled diameter is slightly larger than the optical FOV; only the region where the optical FOV overlaps the detector is defined as IF. The corners of the detector are therefore considered to be OOF. The portion of the field that is inside the optical FOV but outside the detector array is considered to be OOF, too, as it is not part of the image recorded. Here, we consider the OOF for fields up to an elevation of 63 deg as this is the maximum angle at which the Earth is visible. The different frontiers described here are shown in Figs. 1(b) and 1(c), on a polar graph,

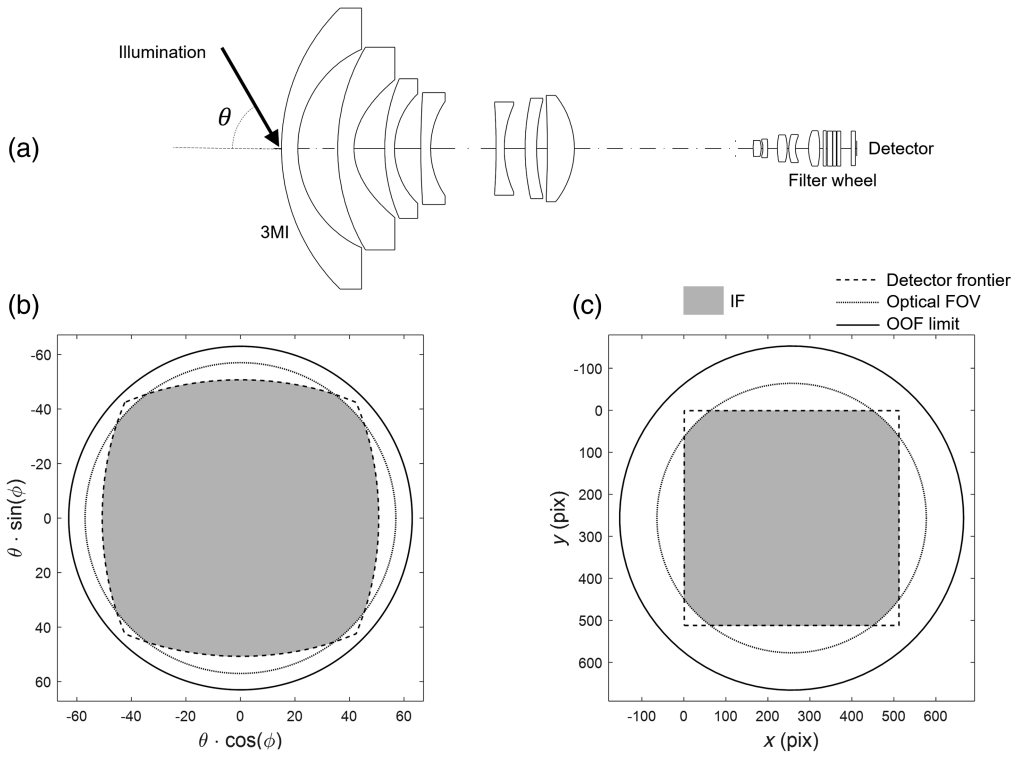

Fig. 1 (a) Sketch of the 3MI optical system. (b) IF and OOF frontiers on a polar grid, with θ and φ, the elevation and azimuth angles, respectively. (c) IF and OOF frontiers at the detector level. The IF is the gray area.

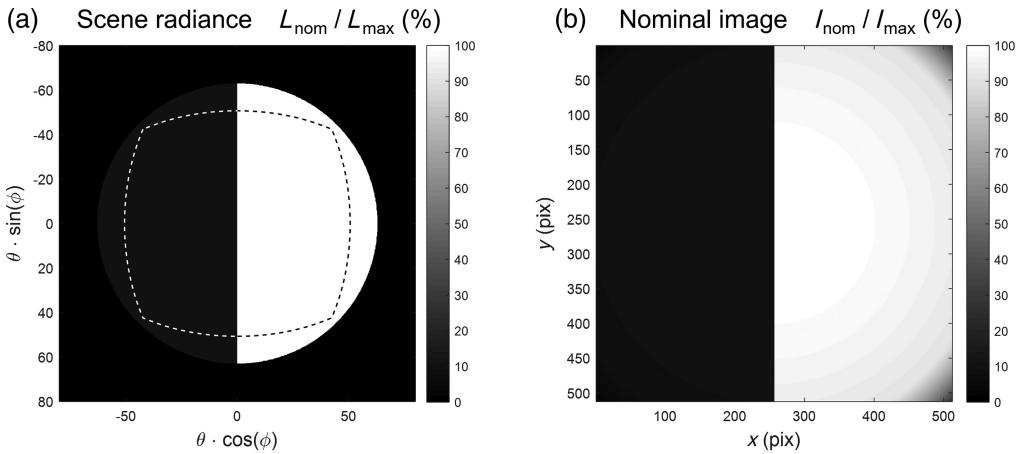

Fig. 2 (a) Radiance of the B&W extended scene. (a) Nominal image at the detector for the B&W extended scene illumination.

where θ and ϕ are the elevation and azimuth angles of the input field (b) or at the detector level (c), respectively, and the gray area is the IF.

SL performance for Earth observation instruments is often evaluated based on a reference black and white (B&W) extended scene.[5,8,19] This consists of illuminating one side of the FOV with a bright uniform radiance L_{max} ($W/m^2/sr$) and the other side with a dark radiance L_{ref}. Figure 2(a) shows the B&W scene radiance with $L_{ref} = 0.1 \cdot L_{max}$. Figure 2(b) shows the corresponding nominal image (i.e., SL free) at the detector, including the effect of a flat field. The measured signal at the detector in unit of counts, or the digital number, and is directly proportional to the irradiance on the detector (W/m^2). All parameters representing a signal at the detector are labeled with I and can include a subscript, e.g., max or ref. The maps at the detected are presented normalized to I_{max}, which is the signal at the center of the detector when illuminated at L_{max}. In the corners, the signal drops very fast to zero as light is vignetted above the optical FOV. No vignetting is present in IF. In the case of IF SL, the performance requirement was a residual SL below $0.017\% \cdot I_{max}$, evaluated at 2σ percentile over the IF area except for the region within 5 pixels from the transition[5] (the requirement area). The 2σ percentile corresponds to a statistical evaluation of the performance on 95% of the pixels, removing potential outliers. Although there was initially no requirement regarding OOF SL correction, we target the same requirement for OOF as for IF, the ideal being if OOF SL could be made much smaller. In the next sections, we present the OOF SL correction approach and performance estimation for 3MI. This work is demonstrated based on SL ray tracing simulations performed at 410 nm considering SL formed by ghosts up to the second order, by far the most dominant kind of SL in the system. This choice of the wavelength was made because it is the smallest wavelength of 3MI, where the SL is expected to be the largest. The SLEP method[20,21] is used for efficient ray tracing.

2 Stray Light Simulation

2.1 Method

When the instrument is illuminated by a scene with radiance $L_{nom}(\theta, \phi)$, the image at the detector (I_{mes}) is the sum of the nominal image (I_{nom}), IF SL ($I_{SL\,IF}$) and OOF SL ($I_{SL\,OOF}$) [Eq. (1)]. Here, all parameters are in units of digital numbers as they represent a signal at the detector. The spatial point source transmittance map, labeled $SPST_{ij}$, is defined as the SL pattern at the detector for a point-like source illumination at field (i, j), such that $I_{nom}(i, j) = 1$. A non-polarized input source is used to avoid unwanted polarization effects in the SPST. The product of $SPST_{ij}$ by $I_{nom}(i, j)$ then gives the SL contribution from field (i, j), and a linear combination over $i, j = [1:N]$ gives the total IF SL [Eq. (2)].[5] Here, $x, y = [1:N]$ are the spatial coordinates on the detector array, in units of pixels

$$I_{mes}(x, y) = I_{nom}(x, y) + I_{SL\,IF}(x, y) + I_{SL\,OOF}(x, y), \quad (1)$$

$$I_{\mathrm{SL\,IF}}(x,y) = \sum_{i,j=1:N} \mathrm{SPST}_{i,j}(x,y) \cdot I_{\mathrm{nom}}(i,j). \tag{2}$$

Equation (2) cannot be used to compute $I_{\mathrm{SL\,OOF}}$ as no nominal signal is obtained for OOF sources. However, an analogous equation can be written. We define $\mathrm{SPST}^*_{\theta,\phi}$ as the SL map for a point-like source illumination at field (θ,ϕ), when the input beam has an input irradiance $E_{\mathrm{input\ col}} = 1\ \mathrm{W/mm^2}$ in the plane normal to its direction. The OOF SL can be computed with Eq. (3), where the $\mathrm{SPST}^*_{\theta,\phi}$ maps are modulated by the irradiance $E_{\mathrm{input}}(\theta,\phi)$ and summed over a field grid ζ. The expression is rewritten as Eq. (4), where the scene radiance $L_{\mathrm{nom}}(\theta,\phi)$ is multiplied by $\Omega_{\theta,\phi}$, the projected solid angle sustained around (θ,ϕ). Although Eqs. (3) and (4) are valid for both IF and OOF SL, Eq. (2) is more practical for IF as it does not require transforming I_{nom} into a radiance map or computing the solid angle

$$I_{\mathrm{SL\,OOF}}(x,y) = \sum_{\theta,\phi\in\,\zeta} \mathrm{SPST}^*_{\theta,\phi}(x,y) \cdot E_{\mathrm{input}}(\theta,\phi), \tag{3}$$

$$= \sum_{\theta,\phi\in\zeta} \mathrm{SPST}^*_{\theta,\phi}(x,y) \cdot L_{\mathrm{nom}}(\theta,\phi) \cdot \Omega_{\theta,\phi}. \tag{4}$$

Equation (4) can be evaluated over any grid ζ, that is sufficiently dense and for which $\Omega_{\theta,\phi}$ is adapted accordingly. We select a regularly spaced grid on $[\theta\cdot\cos(\phi), \theta\cdot\sin(\phi)]$ (polar graph), as shown in Fig. 3(a)]. In that case, the projected solid angle $\Omega_{\theta,\phi}$ is independent of the azimuth ϕ and presents a relatively small variation with the elevation θ. Figure 3(b) shows its evolution with the elevation, normalized to its maximum value Ω_0 defined by Eq. (5), where di is the grid sampling in the polar graph expressed in degrees. Another possible grid would be one defined as being regularly spaced at the detector level, in which the distortion curve is extrapolated for elevations larger than the optical FOV. This is the grid implicitly considered in Eq. (2). For OOF SL computation, this grid is not practical as the solid angle varies both in azimuth and elevation. Moreover, over a polar graph, this grid has a significantly larger density for large elevations, where the OOF SL is the smaller, as we will show. To the best of our knowledge, it is not possible to build a regularly spaced grid with a constant solid angle

$$\Omega_0 = \left(di \cdot \frac{\pi}{180}\right)^2. \tag{5}$$

In the case of TIRS, the SL kernel with an illumination of the instrument over a finite solid angle instead of a point-like source illumination[13,14] (equivalent to $\mathrm{SPST}^*_{\theta,\phi}\cdot\Omega_{\theta,\phi}$) is considered. Therefore, the OOF SL is computed based on a simple modulation of the SL kernel by the scene radiance. This is possible because the SL kernel is obtained by reverse ray tracing simulations,[13,14] in which the solid angle is automatically taken into consideration. With experimentally

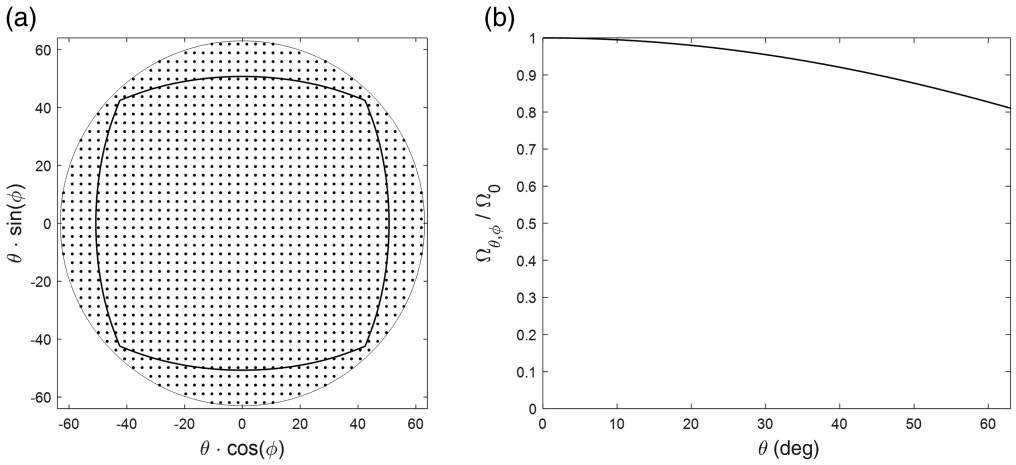

Fig. 3 (a) Regularly spaced grid on a polar graph and (b) corresponding solid angle as a function of the elevation.

calibrated maps, point-like source illumination is preferred as it would be extremely complicated to adapt the source solid angle for each field of the grid.

2.2 Stray Light in 3MI

Figure 4(a) shows the average value of the SPST* in 3MI (<SPST*>) as a function of the azimuth and elevation angles. The dotted line represents the frontier of the detector array. The average is computed over all pixels of the detector array within the IF area (i.e., without the corners). Figure 4(b) shows the average SPST* as a function of the elevation, for azimuth angles between 0 deg and 360 deg. As the graphs in Figs. 4(a) and 4(b) show, the OOF SL is significantly smaller than the IF SL. In the case of IF illumination, it was shown that up to 90% of the SL comes from ghosts generated after the aperture stop and are mostly localized around the nominal pixel.[20] For OOF illumination, light is vignetted by the front baffles or the aperture stop; therefore, significantly fewer ghosts are formed.

Figure 4(c) shows SPST* maps for different elevations in 3MI, with an azimuth angle $\phi = 0$ deg in each case. Many ghosts are present over the detector for IF illumination at $\theta = 0$ deg and 50 deg. As $\phi = 0$ deg, the map at $\theta = 54$ deg corresponds to OOF illumination even if contained inside the optical FOV. In that case, the aperture stop does not introduce vignetting, and many ghosts are present. Nevertheless, the most intense ghosts fall outside the detector array; therefore, the average value over the detector is decreased. At an elevation of 56 deg, which is still within the optical FOV, the light is vignetted by the front baffle due to its asymmetric shape, and the number of ghosts is reduced. At 60 deg, the source is outside the optical FOV and is thus vignetted by the aperture stop, producing even fewer ghosts on the detector.

Figure 5 shows the IF (a) and OOF (b) SL at the detector when the instrument is illuminated with the B&W extended scene from Fig. 2(a). Table 1 gives the SL level inside the requirement area. Although ultimately the performance will be evaluated at 2σ percentile, other statistics are presented as well. It should be noted that the IF values here are slightly different than those presented in the paper related to IF correction,[5] this difference comes from the flat field effect being previously neglected. As the table shows, the OOF SL from the extended scene is about 1 order of magnitude below the contribution from IF SL. Therefore, the OOF SL correction factor

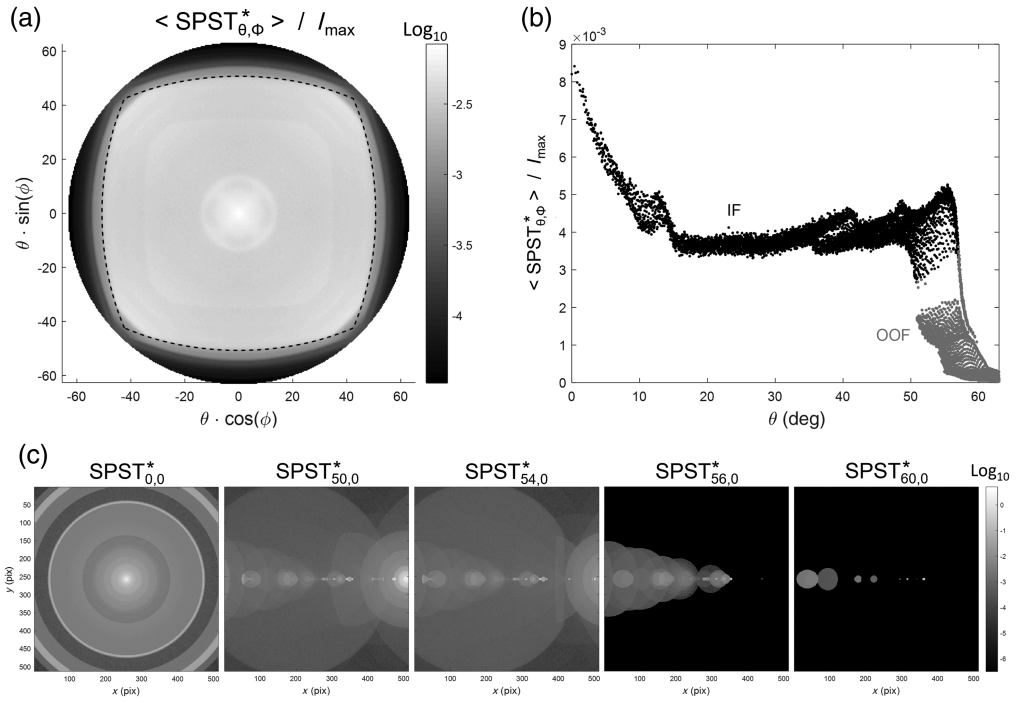

Fig. 4 (a) <SPST*> as a function of the elevation and azimuth. (b) <SPST*> as a function of the elevation for all azimuth angles. (c) SPST* for different fields, with constant azimuth angle of 0 deg and elevation angle from 0 deg to 60 deg.

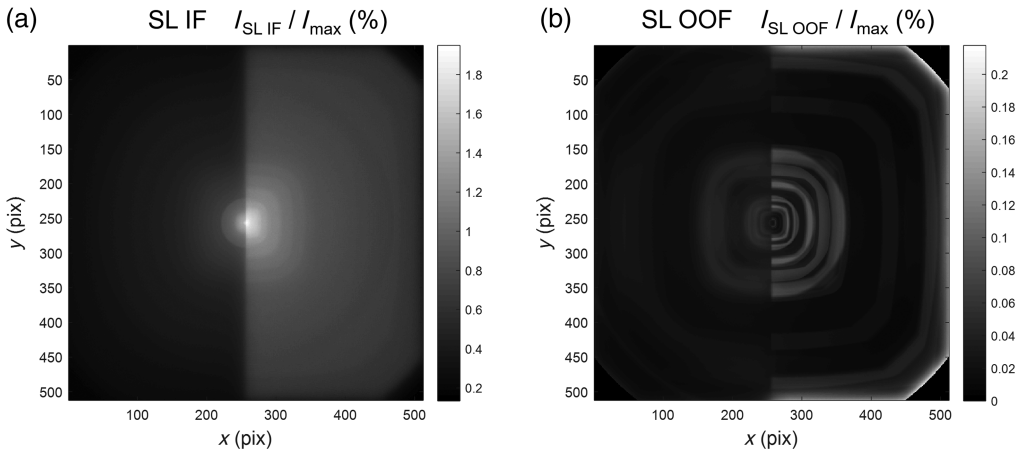

Fig. 5 IF SL (a) and OOF SL (b) in 3MI.

Table 1 SL properties for the B&W extended scenes, estimated on the requirement area.

	$\frac{I_{SL}}{I_{max}}$ (%)	$\frac{I_{SL\,IF}}{I_{max}}$ (%)	$\frac{I_{SL\,OOF}}{I_{max}}$ (%)	$\frac{I_{SL\,IF}}{I_{SL\,OOF}}$
1σ	0.7148	0.7003	0.0262	26.7
2σ	1.0054	0.9577	0.0702	13.6
3σ	1.3935	1.3474	0.1373	9.8
Mean value	0.5876	0.5598	0.0278	20.1

does not need to be as large as for IF SL. A factor of 4.1 is sufficient for reaching a residual OOF SL of 0.017% I_{max} at 2σ.

3 Stray Light Correction

3.1 Principles

The proposed approach for SL correction is to start by estimating the OOF SL contribution and to remove it from the measured signal I_{mes}. Then, the IF correction[5] can be applied on the resulting image. Ultimately, the residual SL is the sum of the OOF residual error and the IF residual error. To be precise, the presence of residual OOF SL affects the estimation of IF SL. However, this is negligible if residual OOF SL is small compared to the nominal signal.

A large number of SPST* maps needs to be characterized to estimate the SL over a dense grid. However, SPST* calibration is time consuming; thus, only a limited number of maps can practically be measured. Therefore, maps are calibrated for fields regularly spaced on the polar grid with a realistic sampling $di_c = 1.94$ deg. Moreover, the calibration is restricted to azimuth angles between 0 deg and 45 deg (total of 117 maps) as the maps for azimuth angles between 45 deg and 360 deg can be derived by symmetry. Calibration only along the radial direction would have not been sufficient as the detector is square. For the SL correction, Eq. (4) is then used to estimate the OOF SL based on these calibrated maps.

The SL correction performance can be improved by interpolating the calibrated SPST* maps to a denser grid. The correction grid sampling is therefore reduced from di_c to di. Previously, a scaling interpolation method was developed for IF SL in 3MI, where the SPST map at a given field is obtained by applying a rotation and scaling operation to the map calibrated at the closest field.[5] The rotation is the difference in azimuth angle between the field to interpolate and its closest neighbor. The scaling is the ratio between the radial distance of the nominal pixel of both fields. Up to four neighbors are considered to avoid missing signal in the corners. A similar method can be applied for OOF maps by considering a scaling by the ratio of their elevation. This

interpolation method, based on a local symmetry assumption, exhibits some deviation from the theoretical map. The denser the calibration grid is, the more accurate the interpolation becomes.

Spatial and field binning can be used to decrease the amount of data. Spatial binning consists of reducing the spatial dimension of individual SPST* maps from $N \times N$ to $n \times n$. Spatial binning affects the SL correction accuracy; however, it was shown that it can be used to attenuate high spatial frequencies that appear in the SL estimation when using a low density correction grid.[5] The spatial binning that minimizes the SL error for a given grid sampling is called the "optimal" spatial binning (see Appendix 1). Field binning consists of averaging the maps associated with adjacent fields. It reduces the number of maps used for the correction in Eq. (4) and, therefore, increases its sampling from di to a larger value df. Field binning has the same consequence as if the SL was computed with sampling di but with a scene radiance known with a sampling df.[5]

An important unknown for the SL correction is the scene radiance L_{nom}. Indeed, with a single shot measurement, the OOF nominal image is not measured. We describe in Sec. 3.3 how it can be estimated. For now, we assume that we know the scene radiance, and we evaluate the SL performance on the B&W extended scene to tune the parameters.

3.2 B&W Scene Performance

Figure 6(a) shows the OOF SL for the B&W extended scene, estimated with $di = di_c = 1.94$ deg. The estimation is computed with the calibrated maps without an intermediary interpolation step. Because of the low density grid, localized ghosts from individual SPST* maps can be distinguished on the image. This effect can be attenuated with an optimal spatial binning ($N/n = 8$), as shown in Fig. 6(b). A better estimation of the SL would be obtained if the maps were calibrated over a denser grid. This is shown in Fig. 6(c), where the estimation is performed with maps calibrated on a grid with smaller sampling, $di = di_c = 0.65$ deg. In that case, the optimal binning is smaller ($N/n = 2$); the resulting map is shown in Fig. 6(d).

The continuous curve in Fig. 7 shows the SL estimation error dSL (evaluated at 2σ in the requirement area) as a function of di, assuming a calibration of the maps for all fields of the correction grid (i.e., $di_c = di$). For each value of di, we apply the optimal binning that minimizes dSL (see Fig. 11 in Appendix 1). The graph shows that the error decrease when di is reduced but that we do not reach the performance requirement with the realistic calibration sampling ($di_c = 1.94$ deg). Consequently, interpolation of the SPST* maps is required to reach a satisfactory performance.

The dotted curve in Fig. 7 shows the error dSL when maps are calibrated on a grid with sampling $di_c = 1.94$ deg and that interpolation is performed to a correction grid with sampling di. Also, the optimal binning is applied for each value of di. As can be seen, the interpolation of the maps reduces the error below the performance requirement. However, the interpolation process introduces an error on each SPST* map; therefore, the value dSL is not as good as if theoretical maps were considered. With an interpolation to $di = 0.65$ deg, the residual SL error is nearly half of the requirement. Figure 6(e) shows the estimated OOF SL in that case, and Fig. 6(f) shows the application of the optimal spatial binning. Visually, it looks very similar to the theoretical situations shown in Figs. 6(c) and 6(d). For more details, Fig. 12 and Table 3 in Appendix 2 show the residual error map and statistics for $di = di_c$ and $di = 0.65$ deg.

The impact of field binning depends on the scene but is usually limited, as discussed in a previous paper.[5] Figure 13 in Appendix 3 shows that the OOF SL correction error with the B&W extended scene remains significantly lower than the IF requirement even for large field binning (i.e., df small). Indeed, the impact of field binning is that SPST* maps are modulated by a smoothed input scene. For the B&W scene, this leads to errors only for SL coming from the transition area.[5] A best practice is to consider a field binning with df as close as possible to di within available computation capabilities. Ultimately, maps will be calibrated on a grid with $di_c = 1.94$ deg, interpolation will increase the density with $di = 0.65$ deg, and field binning will bring back the sampling to $df = di_c$.

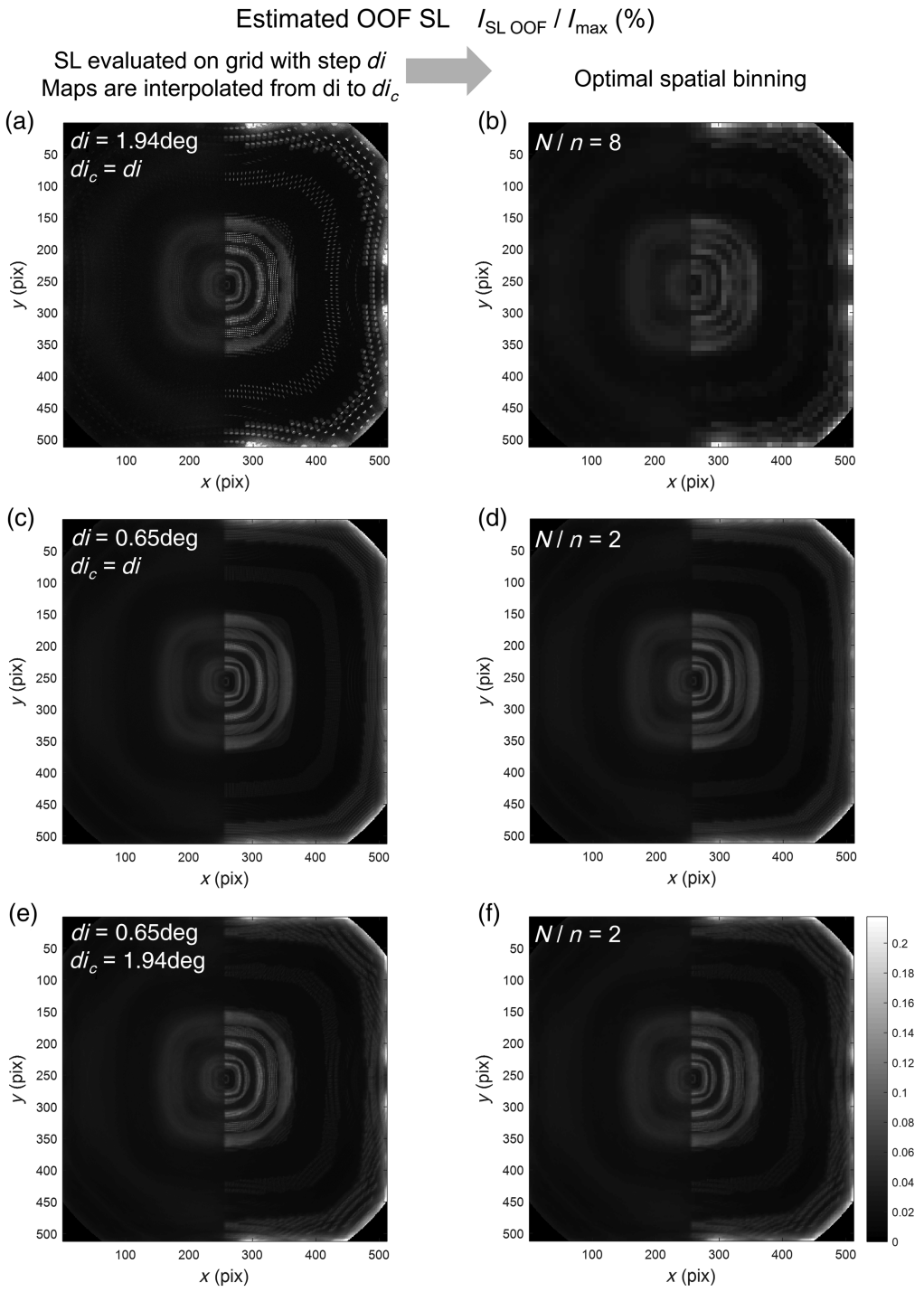

Fig. 6 OOF SL estimated with SPST* maps known on a calibration grid di_c and interpolated to *di*. Maps (a), (c), and (e) are computed in high spatial resolution, and an optimal spatial binning is applied to maps (b), (d), and (f).

3.3 Input Scene Radiance Estimation

With a single shot image acquisition, the OOF scene radiance (L_{nom}) is unknown. However, an estimation of the scene radiance (L_{est}) is necessary to compute the OOF SL. Montanaro et al.[13] proposed deducting the OOF radiance with an external sensor acquiring coincident data. However, this is challenging operationally,[13] and data are not necessarily available at the desired spectral range. Another approach is to take advantage of the instrument push broom configuration for reconstructing the OOF scene in the along-track (ALT) direction. Indeed, the

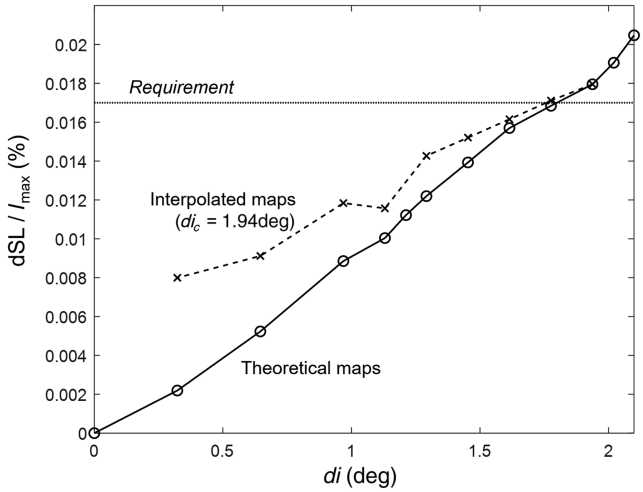

Fig. 7 OOF SL error (estimated at 2σ in the requirement area) as a function of the correction grid sampling *di*. The continuous curve assumes that the maps are calibrated on the correction grid (i.e., $di_c = di$); the dotted curve considers maps calibrated on a grid with sampling $di_c = 1.94$ deg and interpolated to a grid with sampling *di*.

instrument continuously acquires images of the Earth along one direction as it rotates around it. An example is shown in Figs. 8(a)–8(c), with three images of the Earth taken at successive times when the instrument moves along the *y* direction (ALT). The limitation of push-broom reconstruction is that it does not provide information on the OOF radiance in the across-track (ACT) direction.

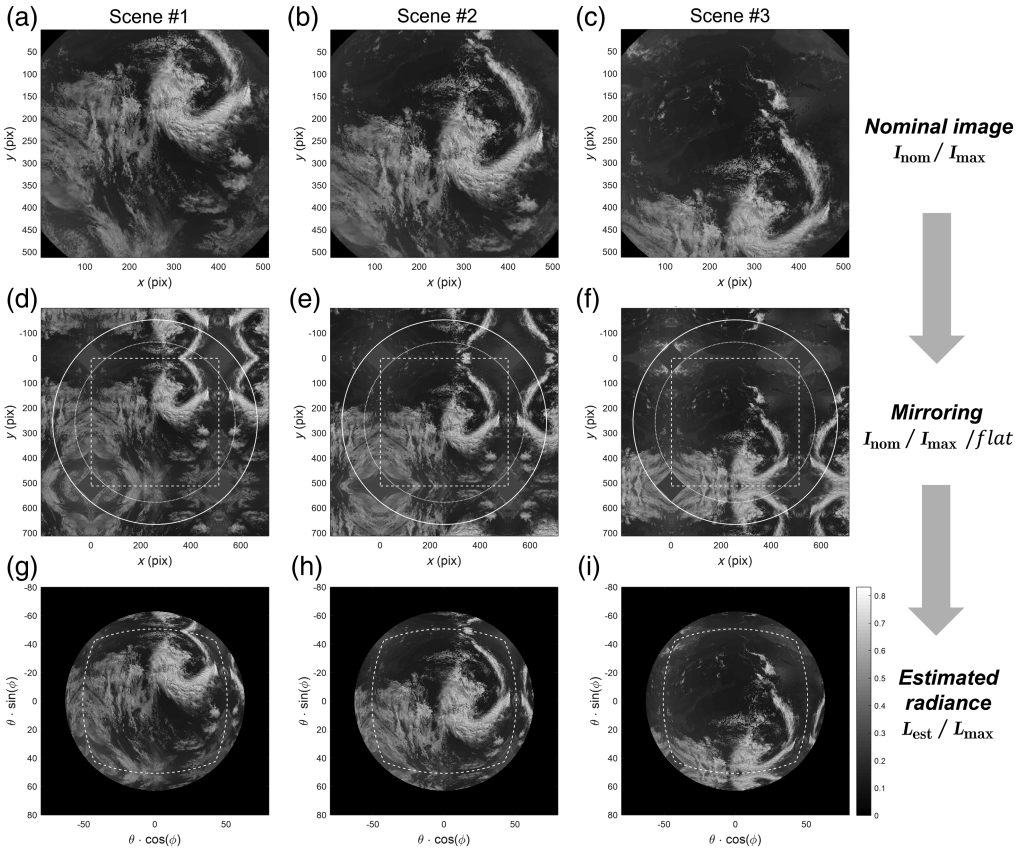

Fig. 8 (a)–(c) Images of the Earth acquired at successive times by an instrument rotating around the Earth in the direction of *y*. (d)–(f) Application of the mirroring at the detector level to estimate the OOF signal. (g)–(i) Conversion of the signal into a radiance and conversion to a polar grid. The input radiance of the OOF scene is obtained in polar coordinates.

The proposed approach for estimating the OOF scene in any direction is to use mirroring. This is shown in Figs. 8(d)–8(f), in which images Figs. 8(a)–8(c), respectively, are corrected from the flat field and then mirrored on each side. Next, the signal is converted into a radiance with the absolute calibration, and the detector grid is converted into angles (θ) due to the distortion curve extrapolated to the OOF region. In the case in which the instrument would present significant gain variations across the detector array, the mirroring should be done preferably after the conversion to radiance. Mirroring results are shown in Figs. 8(g)–8(i).

In the case of 3MI, the corners of the detector are not part of the IF region, and the input light is vignetted. Before applying the mirroring, an average value is thus attributed to the corners. One solution is to attribute the average signal over the IF region of the detector for each corner. However, this is not ideal for high contrast scenes. A better solution is to apply the average value of the pixels in their direct vicinity for each corner.

Mirroring estimates the OOF radiance by assuming a local symmetry in the scene. Therefore, the accuracy of the OOF scene estimation depends on the type of scene. In the simple case of a scene with low contrast or low spatial frequencies, the radiance is quasi uniform, and mirroring gives a quite good estimation of the OOF radiance. This is the case, for example, with the ocean or with extended vegetation areas.

Another situation is when the scene is quite uniform at the exception of a localized feature with high contrast, which is equivalent to the presence of a high frequency. For example, this could be a small cloud or a small island in the middle of the ocean. Under that circumstance, the mirroring of the localized feature is a guess, and its accuracy is a matter of luck. A localized high contrast feature could be missed, or conversely, we could falsely presume the presence of one. This can lead to either the underestimation or overestimation of SL originating from a localized region in the field. As it is only a localized region, it should lead to a small relative error compared with the case in which OOF SL was not corrected.

A third situation is typically the B&W extended scene, which could represent the transition between two high contrast zones such as land and ocean. In that case, the reliability of the mirroring depends on the position and orientation of the transition. For example, a centered transition along the y axis (e.g., Fig. 2) is perfectly mirrored. However, a scene with a curved or tilted transition is subject to mirroring errors. For example, Fig. 9(a) shows the nominal image when the instrument is illuminated by a B&W scene with a transition centered but tilted with respect to the y axis. As shown in Fig. 9(b), the OOF scene estimated by mirroring is perfect everywhere except for the transition, the orientation of which is inaccurate. The error on the OOF radiance is localized and represents a small portion of the OOF. Therefore, OOF SL will be accurately estimated for all angles inside the OOF region except around the transition. Of course, a transition occurring outside the IF region is not possible to predict by mirroring.

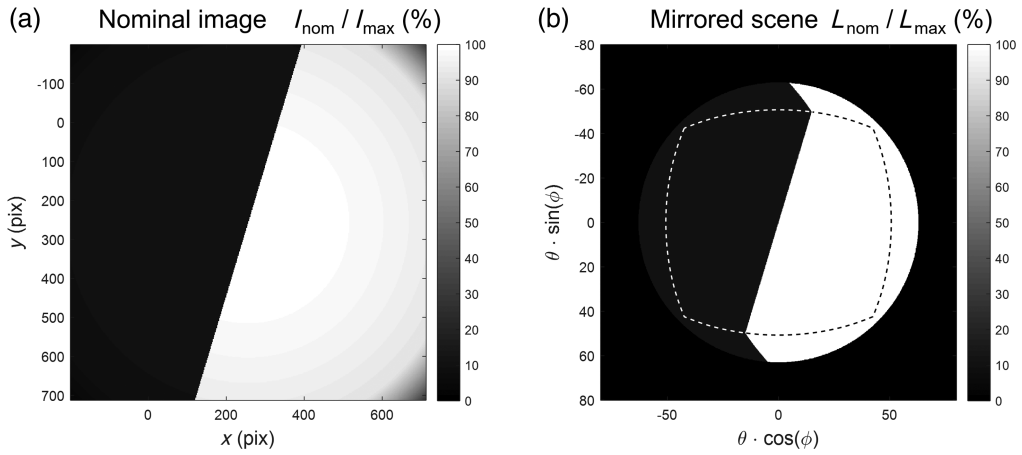

Fig. 9 (a) Nominal image at the detector for a B&W scene with transition tilted with respect to the y direction. (b) The mirroring method estimates perfectly the OOF radiance in the uniform zones, but the transition orientation is not accurate.

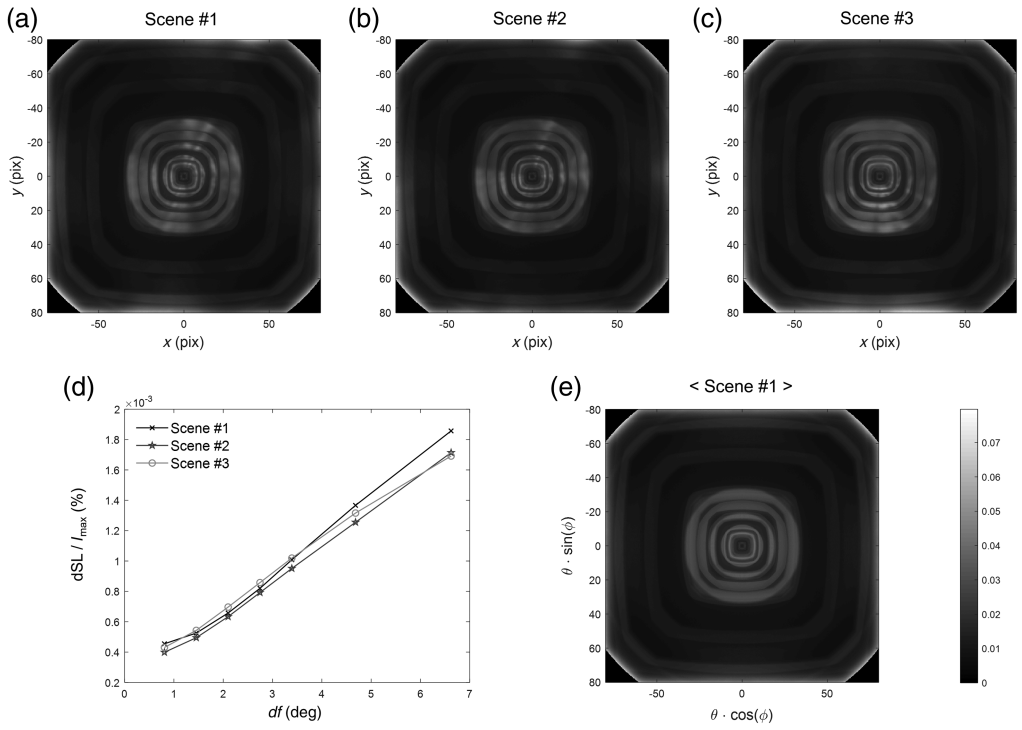

Fig. 10 (a)–(c) OOF SL computed with mirrored OOF radiance of the Earth from Fig. 8. (d) 2σ error introduced on the OOF SL estimation when applying binning compared with the case without binning. (e) OOF SL estimated by averaging the OOF radiance of scene #1.

In particular with a mirrored scene, field binning can be applied with little impact on the SL correction performance. Indeed, field binning smooths the high spatial frequencies of the input scene, where mirroring tends to be least accurate. In regions with low spatial frequencies or low contrast, field binning has little consequence on the radiance; thus, the impact on SL estimation from these regions is limited. In regions with high spatial frequencies or a high contrast transition, field binning can significantly affect the scene. However, mirroring does not accurately predict these features; therefore, field binning does not decrease the accuracy of the radiance from these regions. For example, field binning of the B&W scene of Fig. 9 only impacts the transition zone, which is not accurately predicted by mirroring anyway.

In the case of the three images from the Earth in Fig. 8, the OOF SL computed with the mirror OOF radiance is shown in Figs. 10(a)–10(c), respectively. Despite the presence of a cloud, the scene has few transitions and a limited contrast. Consequently, little deviations are introduced by field binning. Figure 10(d) shows the error dSL on the scene as a function of the binning *df*. The error dSL is estimated at 2σ, comparing the SL with binning and the SL without binning. Although dSL increases with *df*, the error remains small compared with the initial SL, even with strong field binning, as shown in Table 2. Moreover, scene contrast is sufficiently low, so a reasonably accurate estimation of the SL is obtained by averaging the full OOF scene radiance (equivalent to $df = \infty$). This is shown for scene #1 in Fig. 10(e), and the error dSL is given in Table 2. This corresponds to an OOF SL correction by a factor of 5 at 2σ. Nevertheless, in

Table 2 SL properties for the realistic scenes # 1 to 3. The error dSL is the difference between the OOF SL when estimated with field binning compared with the case without field binning.

	Scene #1	Scene #2	Scene #3
$I_{\text{SL OOF}}/I_{\text{max}}(\%)$ **(at 2σ)**	0.0330	0.0308	0.0330
$\text{dSL}/I_{\text{max}}(\%)$ **(at 2σ) with mean OOF radiance**	0.0062	0.0064	0.0072
Ratio	5.3	4.8	4.6

situations in which the scene has higher spatial frequencies and larger contrast, e.g., the B&W scene, averaging the OOF radiance is not acceptable. Hence the choice of df is made based on the B&W scene situation as described previously ($df = 1.94$ deg).

Finally, mirroring is an effective approach for estimating the OOF scene in most situations. Ideally, ALT recombination should be performed in one direction, and the scene in the ACT direction is estimated by mirroring. A limitation of both mirroring and ALT recombination arises when SL originates from the Earth at razing incidence because the Earth's bidirectional scattering distribution function (BSDF) may vary from that at normal incidence.

4 Conclusions

The next generation of space optical instruments is required to have extremely low levels of SL. In Metop-3MI, the presence of many ghosts creates an SL level that necessitates correction through post-processing. Until now, correction algorithms have often focused on SL originating from sources inside the FOV of the instrument. However, significant SL can also emanate from sources located outside the FOV. We developed a method for correcting the OOF SL in 3MI. Similar to the IF correction, the SL map was calibrated using a point-like source at various angles. The SPST* for a given field was obtained by normalizing the SL map to the input radiance. The correction method consisted of estimating the SL, resulting in an illumination of the instrument by a given scene. It was then subtracted from the measured image to get the corrected signal. SL estimation was obtained by a linear combination of the SPST* multiplied by the radiance as well as by the solid angle sustained around the field. The correction can be performed on any grid, so we proposed a arranging the fields on a regularly spaced polar grid. In that case, the associated projected solid angle does not depend on the azimuth angle, and its variation with the elevation is limited. Algorithm parameters were set based on the correction performance for the B&W scene illumination. By calibrating the maps over a grid with sampling $di = 1.94$ deg and interpolating them to a denser grid with $di = 0.65$ deg, the correction on the B&W scene brought the SL level within the scientific requirement limits.

One of the difficulties of OOF SL correction is that the OOF input radiance is unknown. We showed that an effective approach for estimating the OOF radiance was to use mirroring of the IF image. In situations in which the scene has low spatial frequencies and low contrast, mirroring estimated well the OOF scene, on average. In a scene such as the B&W extended scene, mirroring perfectly estimated the radiance in uniform regions, but it was less accurate in predicting the position of transitions. Similarly, mirroring inaccurately estimated the presence of localized high contrast features. Nevertheless, this led to errors on a small portion of the field; therefore, its impact on the OOF SL correction performance was limited. Finally, in the case of Earth observation instruments in a push-broom configuration, the OOF input radiance in one direction was deduced from the recombination of successive images in the along-track direction, whereas mirroring was used in the across-track direction.

This paper utilized ray-traced SPST maps for developing the method's principles, tuning parameters, and predicting correction performance. An experimental calibration of the SPST maps will be conducted prior to launch to provide realistic kernels. This test will take place in a thermal-vacuum chamber, simulating operational space conditions. The correction performance will be verified by illuminating the instrument with an integrating sphere, effectively replicating an extended scene. Post-launch, on-orbit verifications will involve observing well-known terrestrial scenes, such as deserts. Alternatively, observing the moon could provide a well-known reference object.

The approach presented here was developed specifically for the 3MI instrument. However, it has the potential to be applied to a broad range of instruments and various applications. For those instruments sharing a similar architecture and operating principle, such as the OSIRIS airborne instrument, the method could be applied with little or no adaptation. In the case of push-broom telescopes with a single line detector, the method can be adapted by recombining images acquired in the along-track direction and correcting the OOF SL by mirroring in the across-track direction. For instance, we are currently adapting this method for the CLIM mission, which has such a line-detector architecture. In the context of whiskbroom instruments, the OOF SL correction could be similarly applied on images obtained from the combination of consecutive acquisitions in the

along-track direction. For telescopes observing objects other than the Earth, mirroring will not be effective in predicting highly localized objects in space, such as the sun or other celestial bodies. Alternative methods for estimating the nominal OOF radiance could include the use of a scan mirror or acquiring a rough wide-field image with a companion instrument.

5 Appendix A

For any given value of the sampling *di*, there is an optimal value of the spatial binning that minimizes the SL correction error. Figure 11(a) below shows the SL error when considering a sampling $di = 0.65$ deg, for different values of the spatial binning. As can be seen, the error is minimized for an optimal spatial binning of $N/n = 2$. The optimal binning value depends on the sampling *di*, as shown in Fig. 11(b). The smaller sampling and less binning is necessary to minimize the SL error.

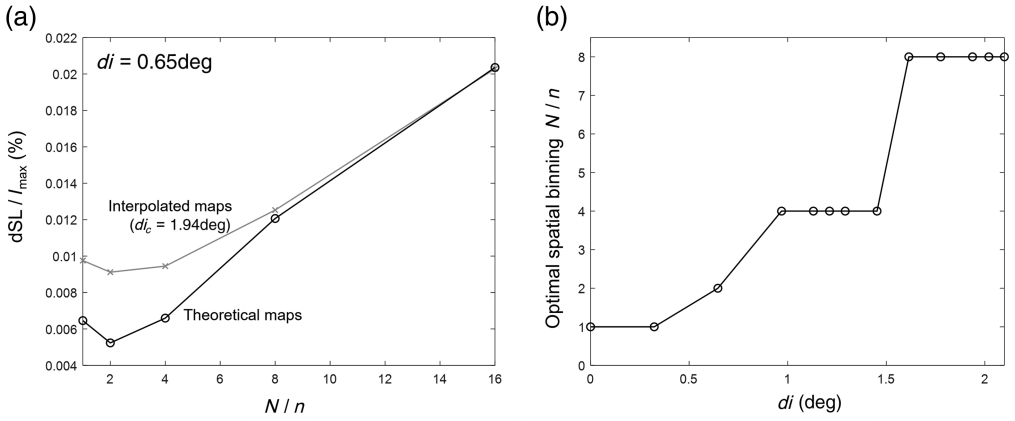

Fig. 11 (a) SL error, dSL, as a function of the spatial binning (*N*/*n*). The dark curve is the error for a scene estimated with theoretical maps on a grid with sampling $di = 0.65$ deg. The light curve is obtained when maps are calibrated with a sampling $di = 1.94$ deg and then interpolated to $di = 0.65$ deg. In both cases, there is an optimal binning that minimizes the error. (b) The optimal binning (*N*/*n*) evolves as a function of *di*. Typically, the larger *di* is, the larger the optimal binning is.

6 Appendix B

Figure 12 shows the residual OOF SL when correcting the SL with SPST* maps calibrated on a grid with sampling $di = 1.94$ deg (a) or with maps interpolated to a denser grid with sampling $di = 0.65$ deg.

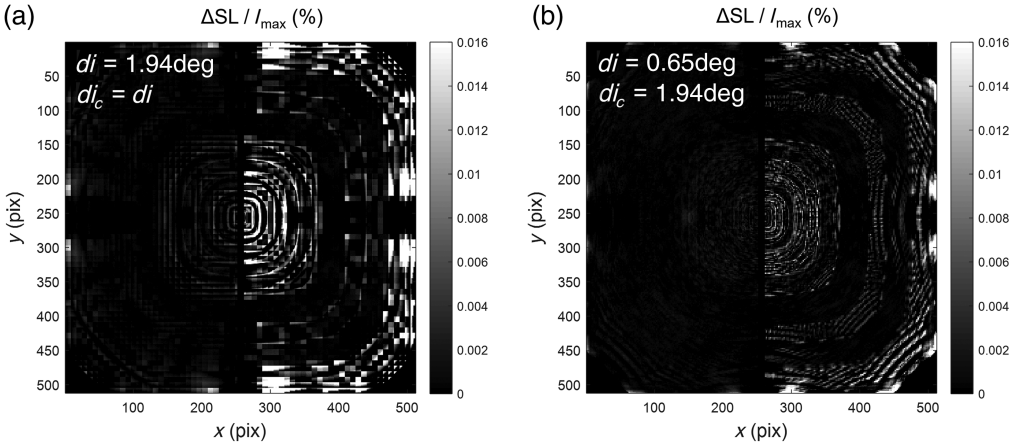

Fig. 12 Residual OOF SL when correcting the SL with maps calibrated on a grid with sampling $di = 1.94$ deg (a) or with maps interpolated to a denser grid with sampling $di = 0.65$ deg. The case in which interpolated maps are used significantly reduces the error, as shown in Table 3.

Table 3 Residual SL after SL correction for two different situations (statistics in the requirement area).

	Residual OOF SL after correction ($\frac{dSL}{I_{max}}$)	
	$di = 1.94$ deg $di_c = di$	$di = 0.65$ deg $di = 1.94$ deg
1σ	0.002%	0.001%
2σ	0.018%	0.009%
3σ	0.064%	0.039%
Mean value	0.004%	0.002%

Table 3 shows the statistics of the residual SL in both cases. The case with no interpolation gives an error at 2σ close to the IF requirement ($dSL \leq 0.017\% \cdot I_{max}$). With interpolation to a denser grid, the error is reduced by half.

7 Appendix C

Field binning only impacts the SL coming from non-uniform zones in the extended scene. For example, if we consider the B&W scene, it only impacts the transition zone. Figure 13(a) shows the field binning applied to that scene, where the left and right sides are unaffected but the transition is smoothed. Figure 13(b) shows the error on the SL estimation due to field binning: we see that the error is only present directly along the transition zone, too. As the transition zone is highly localized, the statistical error over the full detector is small as well, and even with a strong field binning, we conserve a residual SL after correction, which is far below the performance requirement [as shown in Fig. 13(c)].

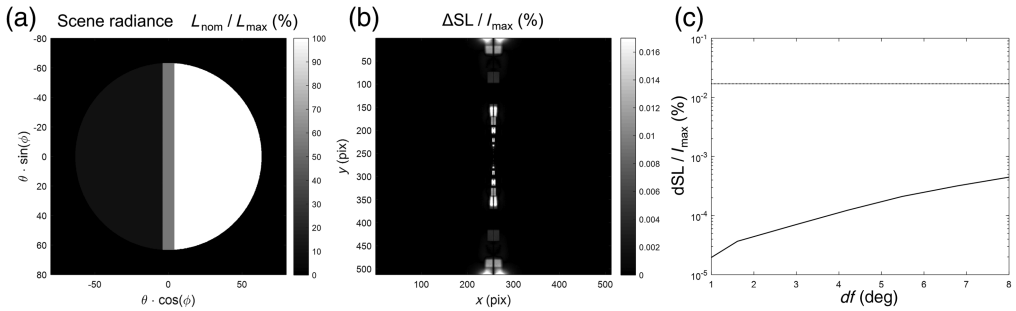

Fig. 13 (a) Field binning of the B&W scene, with an error induced only at the transition zone. (b) Error on the estimated SL when considering the field binning. The error is localized around the transition as the field binning introduces only an error for SL coming from that area. (c) SL error, dSL, as a function of the field binning *df*.

Code and Data Availability

The data that support the findings of this article are not publicly available as they consist of proprietary instrument calibration data of Centre Spatial de Liège and Leonardo Company. They can be requested from the author at lionel.clermont@uliege.be

Acknowledgments

This research was funded by the Leonardo Compact (Grant No. 4500511744/MetOp-SG/CSL). This work is also part of the doctoral thesis of Lionel Clermont, available on the University of Liège repository.[22]

References

1. E. Fest, *Stray Light Analysis and Control*, SPIE Press, Bellingham, Washington (2013).
2. R. Breault, "Control of stray light," Chapter 38 in *Handbook of Optics*, M. Bass et al. Eds., Vol. **1**, pp. 38.1–38.35, McGraw-Hill (1995).
3. J.M. Laherrere, "POLDER on-ground stray light analysis, calibration, and correction," *Proc. SPIE* **3221**, 132–140 (1997).
4. Y. Zong, "Characterization and correction of stray light in optical instruments," *Proc. SPIE* **6744**, 67441L (2007).
5. L. Clermont, C. Michel, and Y. Stockman, "Stray light correction algorithm for high performance optical instruments: the case of Metop-3MI," *Remote Sens.* **14**, 1354 (2022).
6. L. Clermont, "Stray-light calibration and correction for the MetOp-SG 3MI mission," *Proc. SPIE* **10704**, 1070406 (2018).
7. C. Michel et al., "Multi-directional, multi-polarization, multi-spectral imager (3MI) engineering model (EM) on-ground calibration," *Proc. SPIE* **12188**, 121881I (2022).
8. S. Abdon et al., "Digital correction of residual straylight in FLEX images," *Proc. SPIE* **11180**, 111804G (2019).
9. Y. Zong et al, "Correction of stray light in spectrographs: implications for remote sensing," *Proc. SPIE* **5882**, 588201 (2005).
10. Y. Zong et al., "Simple spectral stray light correction method for array spectroradiometers," *Appl. Opt.* **45**(6), 1111–1119 (2006).
11. M. E. Feinholz et al., "Stray light correction algorithm for multichannel hyperspectral spectrographs," *Appl. Opt.* **51**(16), 3631–3641 (2012).
12. M. Montanaro et al., "Stray light artifacts in imagery from the Landsat 8 Thermal Infrared Sensor," *Remote Sens.* **6**, 10435–10456 (2014).
13. M. Montanaro et al., "Toward an operational stray light correction for the Landsat 8 Thermal Infrared Sensor," *Appl. Opt.* **54**(13), 3963–3978 (2015).
14. M. Montanaro et al., "Performance of the proposed stray light correction algorithm for the Thermal Infrared Sensor (TIRS) onboard Landsat 8," *Proc. SPIE* **9972**, 99720F (2016).
15. S. Nevas et al., "Stray light correction of array spectroradiometers for solar UV measurements," *Appl. Opt.* **53I**(19), 4313–4319 (2014).
16. I. Manolis et al., "The 3MI instrument on the Metop second generation," *Proc. SPIE* **10563**, 1056324 (2017).
17. B. Fougnie et al., "The 3MI mission on-board EPS-SG: a multi-spectral multi-polarization multi-directional imager for operational characterization of aerosol and cloud," *Proc. SPIE* **10764**, 107640L (2018).
18. B. Fougnie et al., "The multi-viewing multi-channel multi-polarisation imager - overview of the 3MI polarimetric mission for aerosol and cloud characterization," *J. Quant. Spectrosc. Radiat. Transf.* **219**, 23–32 (2018).
19. V. Kirschner, "Stray light analysis and minimization," Unpublished Tutorial (2017)
20. L. Clermont et al., "Stray light entrance pupil: an efficient tool for stray light characterization," *Opt. Eng.* **59**(2), 025102 (2020).
21. L. Clermont et al., "The stray-light entrance pupil concept and how it can be used to facilitate stray-light characterization," *Proc. SPIE* **11103**, 111030H (2019).
22. L. Clermont, "Stray light control in space instruments: overcoming the conventional limits," Doctoral Thesis, https://hdl.handle.net/2268/260882 (2021).

Lionel Clermont is an optical engineer with expertise in space instrumentation and stray light. Among his experiences, he was responsible for the stray light calibration and correction for Metop-3MI. He is also a pioneer in the development of the time-of-flight (ToF) stray light characterization method and received awards such as the Early Career Achievement award of the International Society for Optics and Photonics (SPIE).

Céline Michel received her PhD from the University of Liège for her work on solar concentrators. She is an optical system engineer, specializing in the on-ground calibration of space optical payloads.